The Astrophysical Journal Letters, 989:L13 (9pp), 2025 August 10 https://doi.org/10.3847/2041-8213/adee05

A Recent Reacceleration of the Local Bubble Revealed by Kinematics of Young Star Associations

Guang-Ya Zeng[1], Guang-Xing Li[1], Bing-Qiu Chen[1], Ji-Xuan Zhou[2], and Martin G. H. Krause[3]
[1] South-Western Institute for Astronomy Research, Yunnan University, Chenggong District, Kunming 650500, People's Republic of China; gxli@ynu.edu.cn, bchen@ynu.edu.cn
[2] School of Physics and Astronomy, Cardiff University, Queen's Buildings, The Parade, Cardiff CF24 3AA, UK
[3] Centre for Astrophysics Research, School of Physics, Astronomy and Mathematics, University of Hertfordshire, College Lane, Hatfield, Hertfordshire AL10 9AB, UK; m.g.h.krause@herts.ac.uk
Received 2025 March 14; revised 2025 July 8; accepted 2025 July 9; published 2025 August 6

Abstract

The low-density region of the interstellar medium where the Sun is located is known as the Local Bubble, a cavity filled with high-temperature and low-density plasma that may be created by a series of supernova (SN) explosions over the past 14 Myr. However, the effects of these SN explosions on the formation and evolution of the Local Bubble, as well as on nearby star formation, remain not fully understood. To study the expansion history of the Local Bubble, we use the kinematic data of the young stars obtained by cross-matching the pre-main-sequence star catalog of E. Zari et al. with the high-precision astrometric and photometric data from the Gaia DR3 database. We perform a 3D spatial clustering analysis on these young stars to identify star associations. We discover three unique star associations that exhibit a wiggle-like velocity pattern. The distances of these star associations are 108.5308, 141.5284, and 176.0318 pc, respectively. Their radial velocities in the local standard of rest are 10.0622, 5.4982, and 9.0581 km s^{-1}, showing a pattern of decreasing and then increasing. This velocity pattern, as predicted by M. G. H. Krause and R. Diehl, is caused by a recent reacceleration affected by the SN explosion, reinforcing the picture of the Local Bubble as an evolving entity.

Unified Astronomy Thesaurus concepts: Pre-main sequence stars (1290); Solar neighborhood (1509)

1. Introduction

Stars directly impact their surrounding interstellar medium (ISM) through the emission of ionizing radiation, stellar winds, and supernova explosions (at the end of the most massive stars' lives). These processes are collectively termed stellar feedback (M. L. M. Collins & J. I. Read 2022). Stellar feedback stands as one of the key drivers of galaxy evolution. It profoundly shapes the structure of ISM, as SN explosions serve as a key source of momentum, energy, and mass reintroduced into the ISM (L. E. Porter et al. 2024).

Stars often form in clusters (e.g., S. S. Larsen 1999; M. G. H. Krause et al. 2020). Thus, bubbles produced by individual massive stars frequently combine into superbubbles. The term is often used in the X-ray community (e.g., B. C. Dunne et al. 2001), where the superbubble becomes X-ray-bright for some time after each supernova explosion inside the superbubble (M. G. H. Krause & R. Diehl 2014; M. Krause et al. 2014). While delivering feedback energy into a common superbubble leads to less radiative cooling compared to individual isolated bubbles, 3D instabilities of the shell lead overall to rapid energy loss (M. Krause et al. 2013; L. Lancaster et al. 2021, 2024). Supershells therefore expand most of the time at moderate velocities, with short-term accelerations when massive stars increase their energy output, e.g., in a supernova explosion. This means that stars formed in or triggered by the shell may, after several Myr have a variety of velocities, and are generally expected to be found inside the superbubble. Note that this is different to outdated 1D superbubble models with continuous energy injection (e.g., R. Weaver et al. 1977), where the supershell continuously decelerates, and thus any stars formed in the shell would keep their formation velocity and outrun the supershell.

The low-density region of ISM where the Sun is located is known as the Local Bubble, filled with low-density and high-temperature plasma detectable by soft X-rays (e.g., D. P. Cox & R. J. Reynolds 1987; W. Liu et al. 2017; X. Zheng et al. 2024). This cavity, which surrounds the Sun, is 100–200 pc wide and is surrounded by a layer of cold, neutral gas and dust (C. Zucker et al. 2022). Measurements of Na I and Ca II absorption lines suggest that the Local Bubble lacks neutral gas (B. Y. Welsh et al. 2010), and the observations in the soft X-ray have verified that the internal temperature of the Local Bubble reaches millions of Kelvin (S. L. Snowden et al. 1997). The conclusive interpretation of all these characteristics is that the Local Bubble was formed by the stellar winds of nearby massive stars and a series of SN explosions over the past 10 Myr (R. K. Smith & D. P. Cox 2001; M. M. Schulreich et al. 2023).

S. Ratzenböck et al. (2023) reconstructed the star formation history of the nearest OB association to Earth, Sco-Cen, by deriving the ages of the 37 clusters selected by the SigMA algorithm. They identified four distinct phases of enhanced star formation activity, which roughly occurred during bursts at 20, 15, 10, and 5 Myr ago. The star formation history of Sco-Cen is dominated by a brief period of star and cluster formation rate at 15 Myr ago. This burst is consistent with the scenario proposed by C. Zucker et al. (2022), which suggests that the Local Bubble was triggered by massive stellar feedback from Sco-Cen.

B. Fuchs et al. (2006) found that young clusters entered the current Local Bubble region around 10∼15 Myr ago and estimated 14∼20 massive members have exploded since that time, through kinematic analysis of the solar neighborhood within 200 pc. D. Breitschwerdt & M. A. de Avillez (2006) have constrained the age of the Local Bubble, according to 19 SN explosions that have occurred to date, to $14.5^{+0.7}_{-0.4}$ Myr through 3D high-resolution hydrodynamic simulations. C. Zucker et al. (2022) also found that the majority of nearby star-forming regions are positioned on the surface of the Local Bubble, indicating that the expansion of the Local Bubble is responsible for triggering nearly all star formation in the vicinity. However, there are still many uncertainties regarding the formation and evolution of the Local Bubble, the process of SN explosions, and their impact on nearby young stars and star formation.

C. Swiggum et al. (2025) performed backward orbital integrations for 509 clusters within 1 kpc of the Sun, tracing their evolution over the past 100 Myr. The majority of the young clusters are divided into three spatial groups, which trace the Pleiades, Coma Berenices, and Sirius moving groups, respectively. They suggest that these young clusters likely formed in massive star-forming complexes, initially moving together with the older stars in the moving groups before gradually separating after the parent gas was expelled by stellar feedback. The kinematic features inherited by the young clusters are likely formed under the influence of Galactic-scale perturbations driven by spiral arms.

Young stars typically form within vast molecular clouds, where they are accompanied by hundreds or thousands of other young stars (M. Kounkel et al. 2022). It is difficult to directly detect the 3D spatial motion of the molecular gas, but since young stars are unlikely to deviate far from their natal clouds and their kinematic information is similar to that of their natal molecular clouds (A. J. Tu et al. 2022), it is feasible to track the motion of these molecular gases based on the kinematic data of young stars born within them. At the same time, as age increases, the "initial" structural characteristics tend to be blurry as a result of n-body interactions among stars. Therefore, the structural and kinematic characteristics associated with molecular clouds are likely to be more pronounced in young star clusters (M. G. H. Krause et al. 2020).

We study the kinematic characteristics of star associations near the Local Bubble by combining the re-main-sequence stars in the re-main-sequence catalog of E. Zari et al. (2018) with the high-precision photometry and kinematic data provided in the Gaia DR3 catalog. The organization of this Letter is as follows. We describe the data sample used in Section 2, present the methods for obtaining the kinematic characteristics of star associations in Section 3, discuss and analyze the results of our work in Sections 4 and 5, and provide a summary in Section 6.

2. Data

The young star sample we use comes from the pre-main-sequence (PMS) catalog of E. Zari et al. (2018), which includes a total of 43,719 sources. They utilized data from Gaia DR2, selecting stars within a 500 pc neighborhood of the Sun. By applying comprehensive constraints on photometric and astrometric parameters, they filtered out early-type stars and PMS stars on the Hertzsprung–Russell diagram, and the sample's extinction correction was made using a 3D g-band extinction map produced by E. Zari et al. (2018).

Compared to Gaia DR2, Gaia DR3 (Gaia Collaboration et al. 2023) is based on astrometric and photometric measurements of over 1.8 billion celestial bodies observed over 34 months, providing higher precision for astrometric parameters such as celestial coordinates, proper motions, parallaxes, as well as photometric parameters across various bands, and also includes a wealth of radial velocity information. We cross-match the PMS catalog of E. Zari et al. (2018) with Gaia DR3 to obtain more accurate data. We select all sources that match the radial velocities from Gaia DR3, amounting to a total of 19,079, which serves as the sample for processing and analysis.

3. Clustering and Kinematic Parameters

To study the kinematic characteristics of star associations and molecular clouds in the solar neighborhood, we perform a clustering analysis on the selected PMS star samples to extract the structures of star associations and assign each PMS star to the corresponding structure.

We use the histogramdd module in Python to create a density map of our samples in the 3D space of Galactic longitude, latitude, and distance. The ranges for each are $0° < l < 360°$, $-90° < b < 90°$, and $1.3 < \log_{10}(d/\mathrm{pc}) < 3.8$. For the density map, we apply a Gaussian filter for smoothing. Partial results are depicted in Figure 1.

For the smoothed density map, we utilize the Dendrogram program from the astrodendro module in Python to extract structures. It offers a straightforward method to compute dendrograms for observational or simulated astronomical data in Python. Like other dendrogram tools, it employs a hierarchical clustering algorithm. The program initially calculates the attribute distance between each pair of classes in the input feature file. It then iteratively merges the closest pair of classes, proceeding to the next closest pair after completion, until all classes have been merged. Ultimately, we identify 263 structures.

Due to the fact that both the method of screening PMS stars and the method of extracting structures can introduce a significant number of contaminating sources, it is necessary to perform a filtering process on the sources assigned to each structure. We employ the method from J.-X. Zhou et al. (2022), which involves verifying the member stars of each structure through the distribution of distances. Ultimately, 180 star association structures remain.

To calculate the kinematic data such as the Galactic coordinates, distance, velocities in different directions, velocity dispersion, local standard of rest (LSR)[4] radial velocity, and peculiar velocities of the identified star associations, we employ various methods. The Galactic coordinates, distance, and velocities in different directions are determined using the average values and standard deviations of the parameters of the member stars within the star association. The velocity dispersion is calculated using the formula $\sigma_v = \sqrt{\mathrm{std}(v_i)^2 - \mathrm{mean}(v_{\mathrm{error},i})^2}$. Here, v_i and $v_{\mathrm{error},i}$ represent the velocities and velocity errors of the member stars in different directions, respectively.

[4] The LSR is a reference frame in astronomy, the motion of which is consistent with the average velocity of all stars within a local region near the Sun (typically within 100 pc or more from the Sun) within the Milky Way.

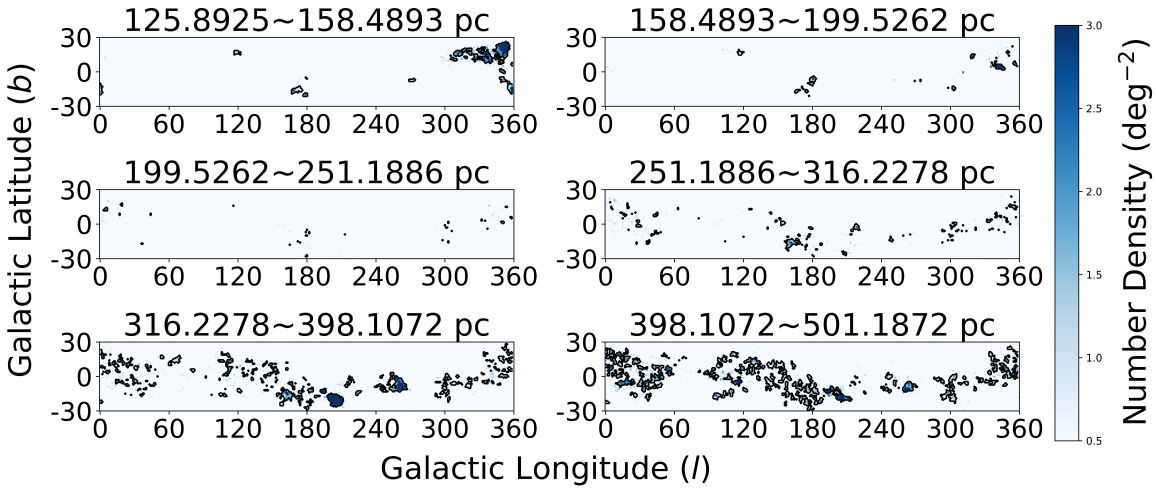

Figure 1. The spatial density distribution of our PMS star sample (a total of 19,079 sources) across partial distance bins, along with the identified star associations. The color represents the number density of PMS stars, with the solid black line delineating the boundaries of the lowest-level substructures found by the dendrogram.

To obtain the LSR radial velocity of the star associations, we calculate the LSR radial velocities of the member stars in the star associations based on the heliocentric radial velocities provided by Gaia DR3, using the formula from M. J. Reid et al. (2009): $v_{r,\mathrm{LSR}} = v_{r,\mathrm{Helio}} + [U_{\odot}^{\mathrm{std}} \times \cos(l) + V_{\odot}^{\mathrm{std}} \times \sin(l)] \times \cos(b) + W_{\odot}^{\mathrm{std}} \times \sin(b)$. The parameters in the formula, $U_{\odot}^{\mathrm{std}} = 11.69\,\mathrm{km\,s^{-1}}$, $V_{\odot}^{\mathrm{std}} = 10.16\,\mathrm{km\,s^{-1}}$, and $W_{\odot}^{\mathrm{std}} = 7.69\,\mathrm{km\,s^{-1}}$, are derived from the results of F. Wang et al. (2021). Then, we use kernel density estimation[5] (KDE) to fit these data and obtain the LSR radial velocity of the association. The kernel function we used is the Gaussian kernel.

We project the 3D LSR velocities of the various star associations onto the dynamical LSR[6] reference frame and the local corotating frame[7] (LCF). In the LCF, the net rotation is removed to reveal shear. Subsequently, we subtract the assumed Galactic shear to reveal the peculiar velocities.

4. Special Star Associations

We discover three unique star associations (named Phantom, Shadow-cluster, and Bubble-edge from near to far) located within the wall of the Local Bubble, including a gasless one. These star associations are spatially close and are the most prominent structures within the region defined by $-90° < l < 30°$, $-60° < b < 60°$, and 80 pc $< d <$ 220 pc (detailed in Appendix B). At the same time, they exhibit a wiggle-like velocity pattern. The distances of Phantom, Shadow-cluster, and Bubble-edge are 108.5305, 141.5284, and 176.0318 pc, respectively, while their LSR radial velocities are 10.0622, 5.4982, and 9.0581 km s^{-1}, showing a pattern of decreasing and then increasing.

Figure 2 shows the distribution of LSR radial velocities for star associations Phantom, Shadow-cluster, and Bubble-edge. We note that all velocity centroids[8] are positive, i.e., outwards, as expected if these stars were produced in the expanding supershell. The left side of Figure 3 shows the distribution of these star associations in the distance (d)–height (z) space, from which it can be seen that Phantom, Shadow-cluster, and Bubble-edge are located at different distances, ranging from near to far, at 108.5308, 141.5284, and 176.0318 pc, respectively. We find that the LSR radial velocities of Phantom and Bubble-edge are higher than the typical expansion velocity of the Local Bubble (6.7 km s^{-1}; C. Zucker et al. 2022). The specific reasons for this situation are explained in Appendix A.

In Figure 4, we illustrate the process of velocity transformation in different reference frames, as described in Section 3, using these unique star associations as examples.

Figure 5 shows the positions of Phantom, Shadow-cluster, and Bubble-edge in the x–y space and their peculiar velocities, as well as their positions in the l–b space, with the right side of Figure 3 showing the distribution of proper motion in the Galactic longitude and latitude directions. It can be seen that although Phantom, Shadow-cluster, and Bubble-edge are very close in space, they still have sufficient separability to be distinguished as different star associations. This property is also reflected in the distribution of proper motion. At the same time, their peculiar velocities and LSR radial velocities exhibit the nature of the Local Bubble's expansion. The elongated, curved nature of Shadow-cluster may be reminiscent of stars that formed in an expanding supershell.

[5] KDE is a common nonparametric estimation method in statistics, used to estimate the probability density function of a random variable. KDE employs kernel functions and, based on a certain bandwidth parameter, estimates the probability density of data points by taking a weighted average of the kernel functions around each data point. In other words, it infers the overall distribution from a finite sample of data.

[6] The dynamical LSR is identical to the LSR, and its motion also follows the average motion of the stars. It is an inertial frame of reference that is transposed continuously along a circular orbit, and on which the acceleration directed toward the Galactic center is eliminated.

[7] The LCF is a reference frame defined by G.-X. Li et al. (2022). Similar to the dynamical LSR, the LCF moves along a circular orbit around the Galactic center. It includes rotation around the Z-axis, which is added to ensure that the x-axis of the frame is locked toward the Galactic center. Due to this, LCF becomes noninertial, and calculations performed in this frame should take into account the Coriolis force. In the LCF, the radial component of the velocity should be consistent with $v_{r,\mathrm{LSR}}$.

[8] The velocity centroid refers to the weighted average of the motion velocity of a system or object within a certain observed velocity space region. It is similar to the concept of the center of mass in space.

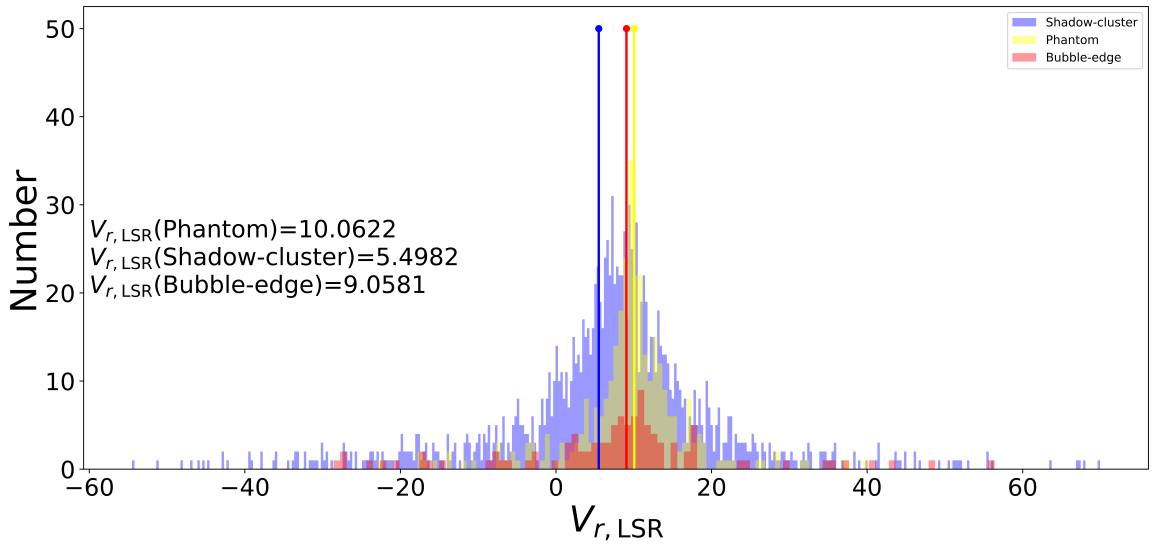

Figure 2. Histogram of the LSR radial velocities of the star association member stars calculated using parameter $U_{\odot}^{\mathrm{std}} = 11.69$ km s^{-1}, $V_{\odot}^{\mathrm{std}} = 10.16$ km s^{-1}, and $W_{\odot}^{\mathrm{std}} = 7.69$ km s^{-1} (F. Wang et al. 2021), with the vertical line (with a dot at the top) indicating the LSR radial velocity of the star association obtained through KDE fitting.

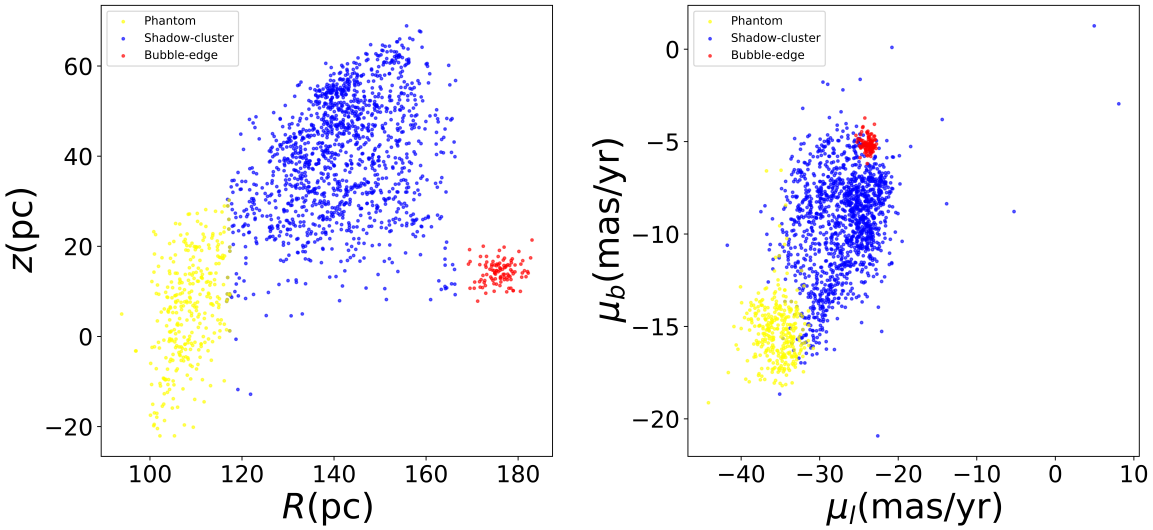

Figure 3. Distribution of the special star associations in the R–z space and the μ_l–μ_b space, with different colors indicating member stars of different star associations.

We compared the kinematic characteristics of these three star associations with the moving groups studied by C. Swiggum et al. (2025), but no one-to-one correspondence was found. At the same time, our sample also has a significant age gap compared to the clusters of C. Swiggum et al. (2025). This suggests that the factors leading to the characteristic velocity distribution do not originate from within the molecular clouds, but are more likely to be caused by external influences.

5. Recurrent Supernova and Wiggle-like Velocity Pattern

Detailed 3D hydrodynamics simulations of SuperBubble (SB) show that supershells decelerate most of the time and experience brief episodes of acceleration after each supernova (M. G. H. Krause & R. Diehl 2014). We propose that these associations may have been influenced by multiple SN explosions during the formation of the Local Bubble. Following the first supernova explosion event, the molecular cloud expands outward under the drive of the ionization front, with its expansion speed gradually decreasing, and stars forming in this process. Due to the diminished influence of SN explosions after the formation of stars, the velocity of star associations stabilizes. Consequently, Phantom and Shadow-cluster formed successively and have essentially maintained the velocities they had at the time of their formation. Bubble-edge likely formed as a result of the second supernova

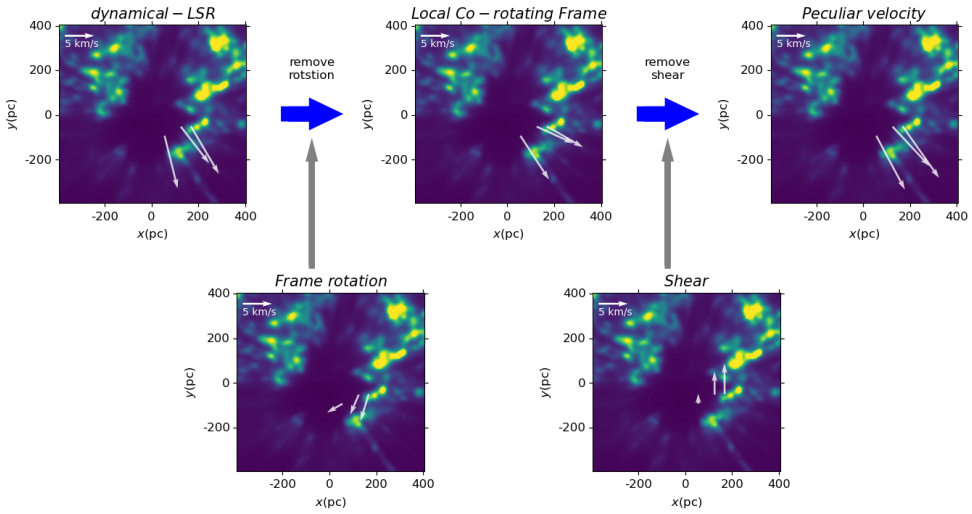

Figure 4. This figure illustrates the process of velocity transformation in different reference frames for these unique star associations, including the dynamical LSR frame, local corotating frame (LCF), and peculiar velocities.

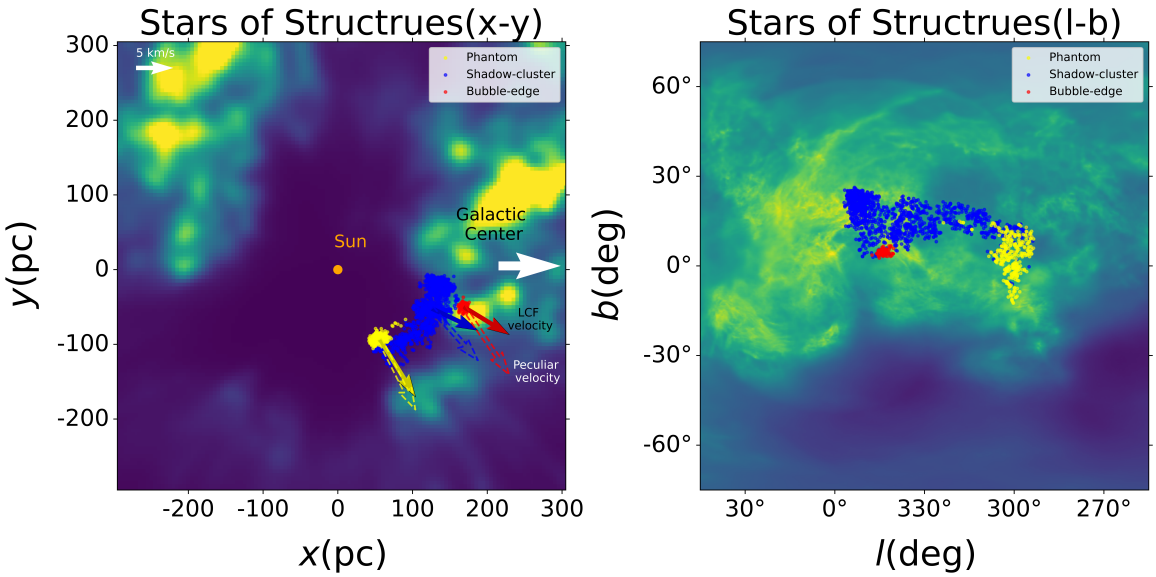

Figure 5. Distribution of special star associations in the *x*–*y* and *l*–*b* spaces, with different colors indicating member stars of different star associations. Arrows indicate the peculiar velocities (hollow arrows) and velocities in the LCF (solid arrows) of the star associations. The orange circle represents the Sun, and the white arrow points toward the direction of the Galactic center. The background of the left figure is the *x*–*y* plane of the 3D (*x*, *y*, *z*) dust image in the solar neighborhood and the background of the right figure is the *l*–*b* plane of the 3D (*l*, *b*, *d*) interstellar dust spatial distribution map drawn by G. Edenhofer et al. (2024).

explosion event. At the time of star formation, the molecular cloud had a higher velocity. This ultimately led to these star associations being close together in space but separated in velocity, creating a wiggle-like velocity pattern. We illustrate this process in Figure 6.

To further confirm the association of these star clusters with SN explosions, we calculated the energy and momenta imparted to the star associations by the combined massive star action (including SN explosions) based on the kinematic parameters of Phantom and Shadow-cluster. As shown in Figure 7, we assumed that the ionization front of the SN explosion was spherical, with the explosion site located 40 pc from Phantom and 75 pc from Shadow-cluster, respectively. We used the basic kinetic energy formula and momentum formula:

$$e = \frac{1}{2}mv^2 \quad (1)$$

$$p = mv \quad (2)$$

$$m = \rho V \quad (3)$$

$$V = 4\pi r^2 d, \quad (4)$$

where the v is the difference in the 3D peculiar velocities of Phantom and Shadow-cluster, which we use to estimate the

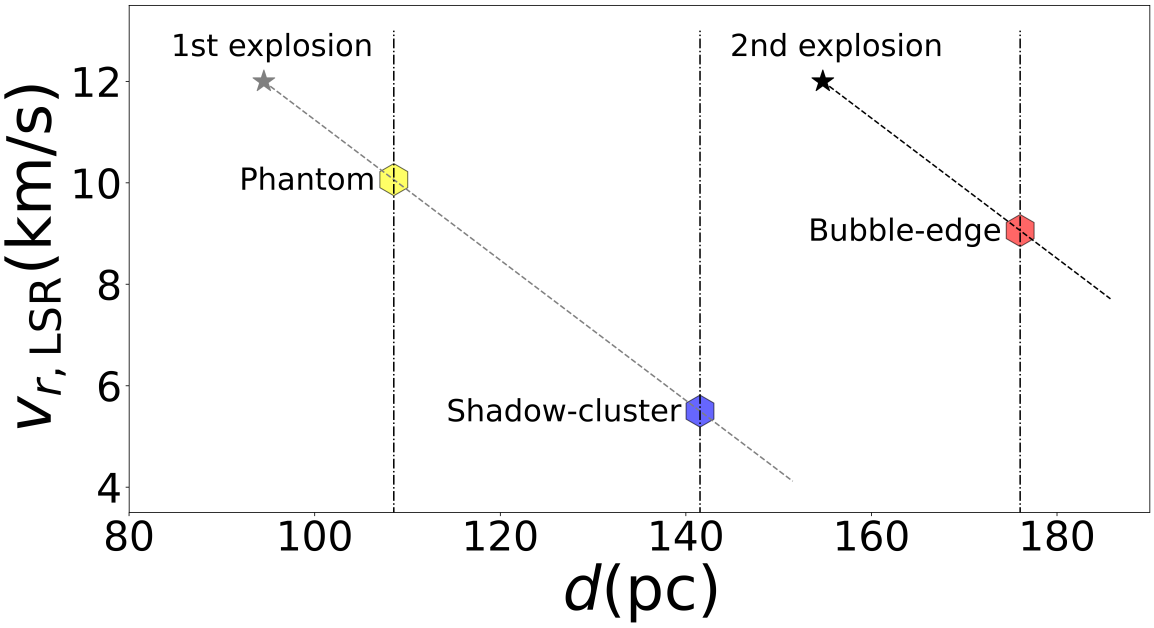

Figure 6. An illustration of our hypothesis that different subassociations within the star associations have been affected by multiple SN explosions. The hexagonal points in different colors represent the various star associations, the gray and black stars denote two SN explosions, and the dashed lines indicate the reduction in molecular cloud velocity after SN explosions and the process of star association formation affected by the SN explosions.

velocity imparted to the molecular cloud by the combined massive star action. We assume that the molecular cloud is blown to a distance of $r = 65$ pc from the center by the combined massive star action, with a cloud thickness of $d = 20$ pc (compare M. Krause et al. 2013), and ρ denotes the density of the H_2 molecular cloud gas. The order of magnitude of the momentum estimation is 10^{40}kg m s^{-1}, and the order of magnitude of the energy estimation is 10^{50} erg.

This order of magnitude estimate agrees well with SB simulations by M. Krause et al. (2013) and M. G. H. Krause & R. Diehl (2014). As Figure 5 in M. G. H. Krause & R. Diehl (2014) shows, the supershell accelerates for a few 10^5 yr after each supernova. The shell velocity reached 8 km s^{-1} in that particular simulation, but would be higher for slightly lower ambient density, for example. Their Figure 2 shows the split into thermal and kinetic energy, showing that about 20% of the supernova energy is expected to be kinetic shell energy in that phase. The shock is expected to run into the clumpy shell, temporarily increasing the density of the clumps further, thus triggering star formation (M. Krause et al. 2013, Figures 5 and 7). We note the energetics of these simulations agree reasonably well with more recent work (compare L. Lancaster et al. 2024).

This discovery reinforces the picture of the Local Bubble as an evolving entity and is significant for filling gaps in research on the formation and evolution of the Local Bubble.

6. Summary

We study the kinematic characteristics of star associations and molecular clouds near the Local Bubble of the Sun by combining the PMS catalog of E. Zari et al. (2018) with the high-precision photometry and kinematic data provided by the Gaia DR3 star catalog in order to test if the PMS associations inside the Local Bubble are consistent with the expectation that they have been formed in the expanding supershell. We plot the density map of the sample and extract the structures, ultimately identifying 180 structures that we certify as star associations. Finally, we calculate the kinematic data for these star associations.

We discover three unique star associations that exhibit a wiggle-like velocity pattern. The distances of Phantom, Shadow-cluster, and Bubble-edge are 108.5308, 141.5284, and 176.0318 pc, respectively, while their LSR radial velocities are 10.0621, 5.4981, and 9.0581 km s^{-1}, showing a pattern of decreasing and then increasing. We believe that they may have been influenced by multiple SN explosions during the formation of the Local Bubble, ultimately leading to this velocity pattern. We have estimated the energy released by the combined massive star action (including SN explosions), and the result's order of magnitude estimate agrees well with superbubble simulations by M. Krause et al. (2013) and M. G. H. Krause & R. Diehl (2014). Our research strengthens the picture of the Local Bubble as an evolving entity and is of great significance for filling the gaps in the study of the formation and evolution of the Local Bubble.

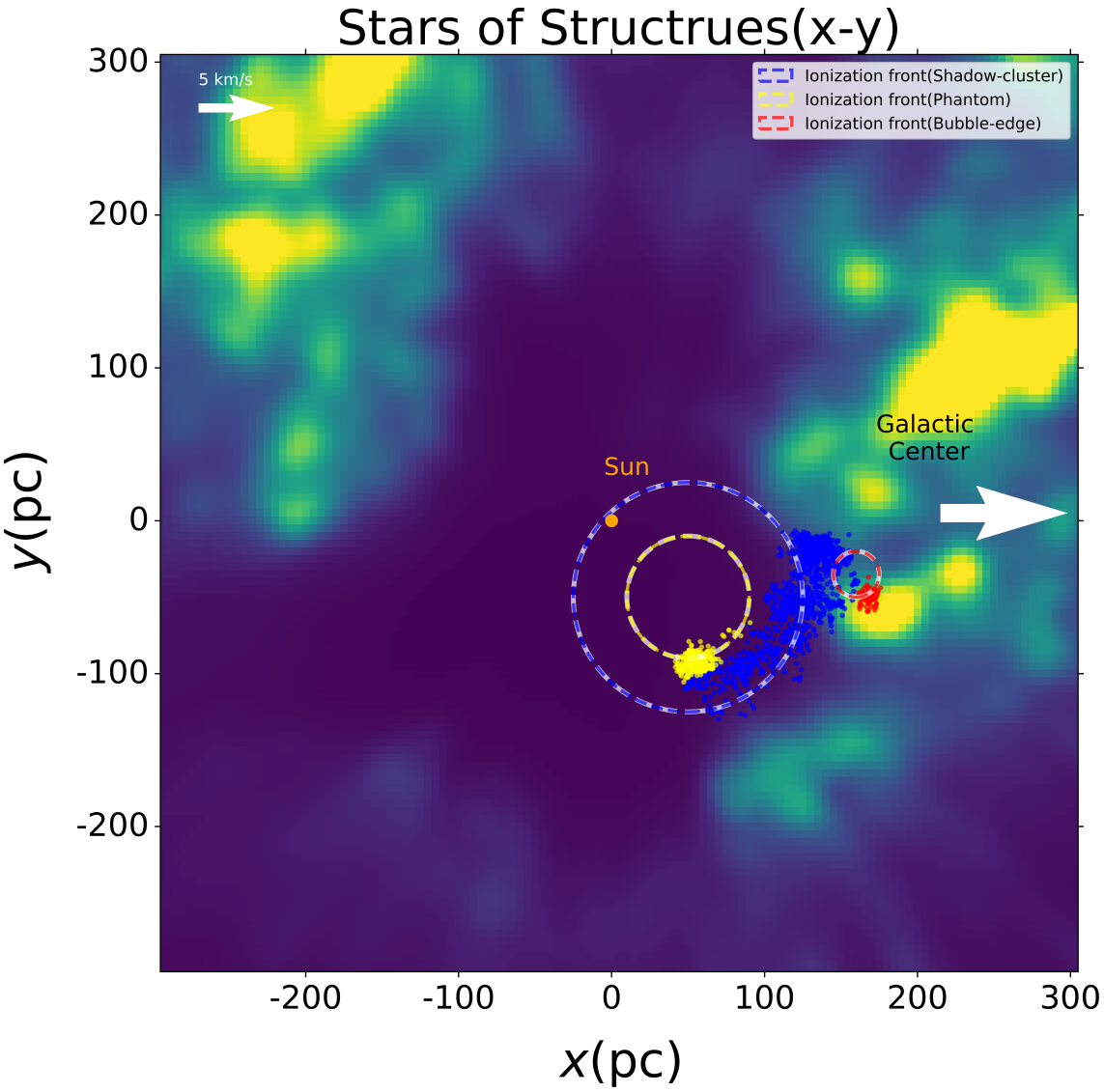

Figure 7. This figure illustrates the assumptions we made during the estimation of the energy released by combined massive star action (including SN explosions). The dashed circles represent the combined massive star action. We infer that the second SN explosion should have occurred between the blue dashed circle and the Bubble-edge.

Acknowledgments

G.X.L. is supported by the National Natural Science Foundation of China 12173034 and 12322304. We acknowledge the science research grants from the China Manned Space Project with no. CMS-CSST-2021-A09, CMS-CSST-2021-A08, CMS-CSST-2021-B03, and CMS-CSST-2025-A11. M.J.H. acknowledges support from the UK STFC [ST/V000624/1]. This work has made use of data from the European Space Agency (ESA) mission Gaia (https://www.cosmos.esa.int/gaia), processed by the Gaia Data Processing and Analysis Consortium (DPAC; https://www.cosmos.esa.int/web/gaia/dpac/consortium). Funding for the DPAC has been provided by national institutions, in particular the institutions participating in the Gaia Multilateral Agreement.

Appendix A
The Higher LSR Radial Velocity

In Section 4, we found that the three special star associations all have LSR radial velocities higher than the typical expansion velocity of the Local Bubble. We believe the reasons should be twofold.

On the one hand, we note that the value from C. Zucker et al. (2022) is not a measurement of the current expansion velocity, but results from a 1D model with substantial idealizations, for example, constant ambient density, energy input just from supernovae, no stellar winds, and 70% of the input energy is radiated away. We use the value, therefore, merely as a typical value over the history of the Local Bubble.

On the other hand, we found that the solar velocity data we used differ from those used by C. Zucker et al. (2022), which

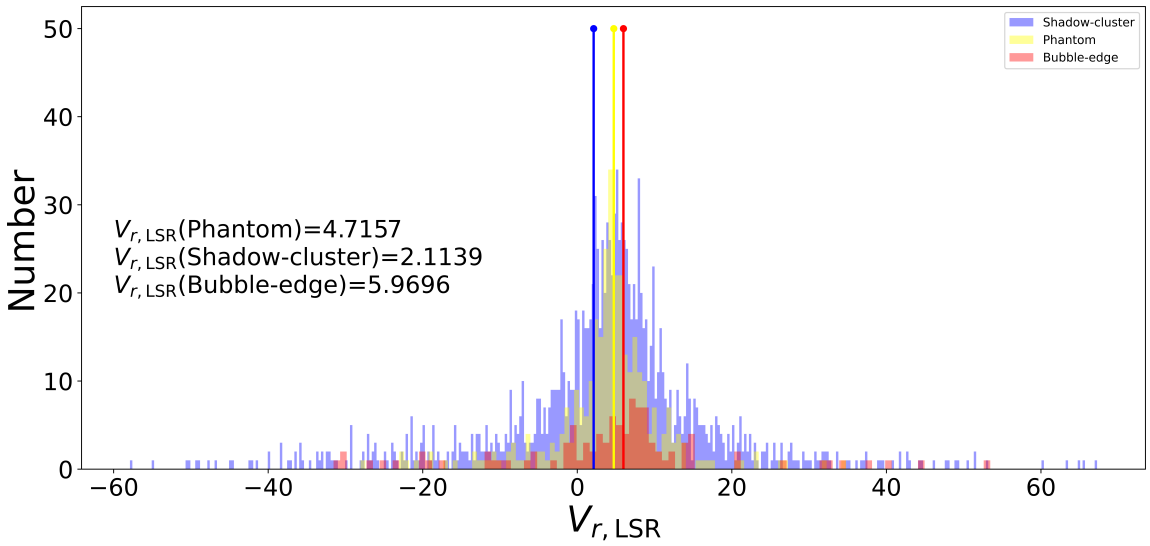

Figure 8. Histogram of the LSR radial velocities of the star association member stars calculated using parameter $U_{\odot}^{\mathrm{std}} = 10.0\ \mathrm{km\ s^{-1}}$, $V_{\odot}^{\mathrm{std}} = 15.4\ \mathrm{km\ s^{-1}}$, and $W_{\odot}^{\mathrm{std}} = 7.8\ \mathrm{km\ s^{-1}}$ (F. J. Kerr & D. Lynden-Bell 1986), with the vertical line (with a dot at the top) indicating the LSR radial velocity of the star association obtained through KDE fitting.

are from F. J. Kerr & D. Lynden-Bell (1986), namely $U_{\odot}^{\mathrm{std}} = 10.0\ \mathrm{km\ s^{-1}}$, $V_{\odot}^{\mathrm{std}} = 15.4\ \mathrm{km\ s^{-1}}$, and $W_{\odot}^{\mathrm{std}} = 7.8\ \mathrm{km\ s^{-1}}$. We present the $v_{r,\mathrm{LSR}}$ calculated using these parameters in Figure 8. We found that these star associations still exhibit a wiggle-like velocity pattern in this case, but their velocities are all lower than the typical expansion velocity of the Local Bubble. The difference in parameters should be the main reason for the significant numerical discrepancy. Considering that the parameters we used are the updated solar motion parameters after Gaia, we believe that our results should be reliable.

Appendix B
Discovery of Special Associations

After calculating the kinematic parameters of the 180 star associations identified by the Dendrogram program, we inspected these star associations to identify objects of interest. In the inspection of the region defined by $-90° < l < 30°$, $-60° < b < 60°$, and 80 pc $< d <$ 220 pc, we focused on the most prominent series of star associations in this region. The Dendrogram program identified three subassociations, and they all belong to the same parent association. We found that

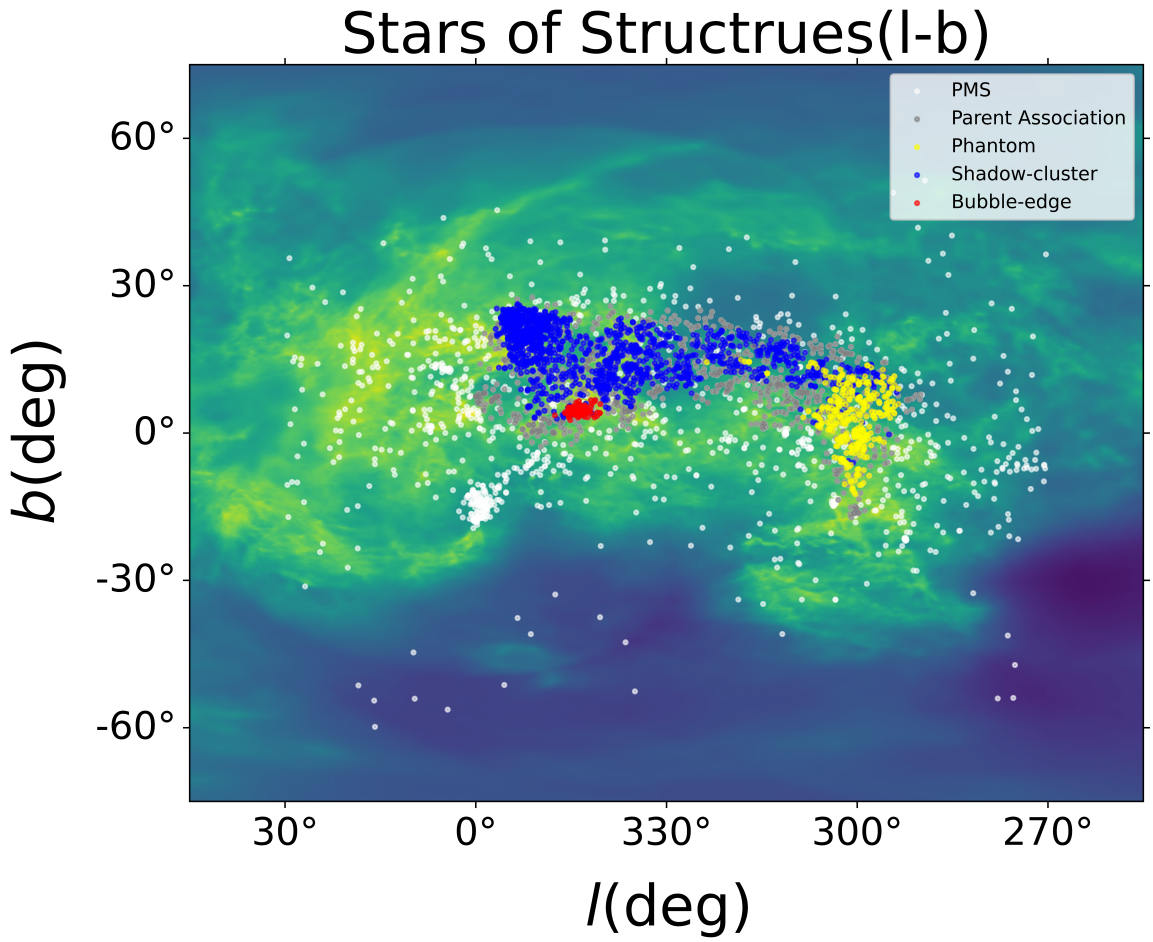

Figure 9. The spatial distribution of the member stars of the parent association and the subassociations, as well as the PMS stars in the region defined by $-90° < l < 30°$, $-60° < b < 60°$, and 80 pc $< d <$ 220 pc.

these subassociations are spatially closely connected but exhibit a wiggle-like velocity pattern in their radial velocity distribution, which is why we are interested in them. Figure 9 shows the spatial distribution of the member stars of the parent association and the subassociations, as well as the PMS stars in this region.

ORCID iDs

Guang-Ya Zeng https://orcid.org/0009-0000-3140-8955
Guang-Xing Li https://orcid.org/0000-0003-3144-1952
Bing-Qiu Chen https://orcid.org/0000-0003-2472-4903
Ji-Xuan Zhou https://orcid.org/0000-0002-1463-9732
Martin G. H. Krause https://orcid.org/0000-0002-9610-5629

References

Breitschwerdt, D., & de Avillez, M. A. 2006, A&A, 452, L1
Collins, M. L. M., & Read, J. I. 2022, NatAs, 6, 647
Cox, D. P., & Reynolds, R. J. 1987, ARA&A, 25, 303
Dunne, B. C., Points, S. D., & Chu, Y.-H. 2001, ApJS, 136, 119
Edenhofer, G., Zucker, C., Frank, P., et al. 2024, A&A, 685, A82
Fuchs, B., Breitschwerdt, D., de Avillez, M. A., Dettbarn, C., & Flynn, C. 2006, MNRAS, 373, 993
Gaia Collaboration, Vallenari, A., Brown, A. G. A., et al. 2023, A&A, 674, A1
Kerr, F. J., & Lynden-Bell, D. 1986, MNRAS, 221, 1023
Kounkel, M., Mcbride, A., Stassun, K. G., & Leigh, N. 2022, MNRAS, 517, 1946
Krause, M., Diehl, R., Böhringer, H., Freyberg, M., & Lubos, D. 2014, A&A, 566, A94
Krause, M., Fierlinger, K., Diehl, R., et al. 2013, A&A, 550, A49
Krause, M. G. H., & Diehl, R. 2014, ApJL, 794, L21
Krause, M. G. H., Offner, S. S. R., Charbonnel, C., et al. 2020, SSRv, 216, 64
Lancaster, L., Ostriker, E. C., Kim, C.-G., Kim, J.-G., & Bryan, G. L. 2024, ApJ, 970, 18
Lancaster, L., Ostriker, E. C., Kim, J.-G., & Kim, C.-G. 2021, ApJ, 914, 90
Larsen, S. S. 1999, A&AS, 139, 393
Li, G.-X., Zhou, J.-X., & Chen, B.-Q. 2022, MNRAS, 516, L35
Liu, W., Chiao, M., Collier, M. R., et al. 2017, ApJ, 834, 33
Porter, L. E., Orr, M. E., Burkhart, B., et al. 2024, MNRAS, 535, 3451
Ratzenböck, S., Großschedl, J. E., Alves, J., et al. 2023, A&A, 678, A71
Reid, M. J., Menten, K. M., Zheng, X. W., et al. 2009, ApJ, 700, 137
Schulreich, M. M., Feige, J., & Breitschwerdt, D. 2023, A&A, 680, A39
Smith, R. K., & Cox, D. P. 2001, ApJS, 134, 283
Snowden, S. L., Egger, R., Freyberg, M. J., et al. 1997, ApJ, 485, 125
Swiggum, C., Alves, J., & D'Onghia, E. 2025, A&A, 699, L5
Tu, A. J., Zucker, C., Speagle, J. S., et al. 2022, ApJ, 936, 57
Wang, F., Zhang, H. W., Huang, Y., et al. 2021, MNRAS, 504, 199
Weaver, R., McCray, R., Castor, J., Shapiro, P., & Moore, R. 1977, ApJ, 218, 377
Welsh, B. Y., Lallement, R., Vergely, J. L., & Raimond, S. 2010, A&A, 510, A54
Zari, E., Hashemi, H., Brown, A. G. A., Jardine, K., & de Zeeuw, P. T. 2018, A&A, 620, A172
Zheng, X., Ponti, G., Freyberg, M., et al. 2024, A&A, 681, A77
Zhou, J.-X., Li, G.-X., & Chen, B.-Q. 2022, MNRAS, 513, 638
Zucker, C., Goodman, A. A., Alves, J., et al. 2022, Natur, 601, 334